Interfacial Reactions and Mechanical Properties Studies of C-Coated and C/B$_4$C Duplex-Coated SiC Fiber-Reinforced Ti$_2$AlNb Composites

Shuming Zhang [1], Minjuan Wang [2], Mao Wen [3], Jianhong Chen [3], Hu Li [2], Chuan Xie [2], Wangtengfei Fan [2], Qingfeng Wang [1,*] and Hao Huang [2,*]

[1] State Key Laboratory of Metastable Materials Science and Technology, Yanshan University, Qinhuangdao 066004, China; smzhang89@yeah.net

[2] AECC Beijing Institute of Aeronautical Materials, P.O.Box: 81-15, Beijing 100095, China; juanjuanyuer@yeah.net (M.W.); lihu989@163.com (H.L.); xiechuan1990@163.com (C.X.); 17888803196@163.com (W.F.)

[3] State Key Laboratory of Superhard Materials, Department of Materials Science, Key Laboratory of Automobile Materials, MOE, Jilin University, Changchun 130012, China; wenmao225@163.com (M.W.); jhchen19@yeah.net (J.C.)

* Correspondence: wqf67@ysu.edu.cn (Q.W.); huanghaoxj@126.com (H.H.); Tel.: +86-1393-356-0072 (Q.W.); +86-1891-072-1253 (H.H.)

check for updates

Abstract: Continuous SiC fiber-reinforced Ti$_2$AlNb matrix composites have a great potential for high-temperature aviation structure applications, and their properties strongly depend on the microstructure of the interfacial reaction layer. Notably, introducing diffusion barrier coatings has still been a popular strategy for optimizing the interfacial structure and interfacial properties of SiC$_f$/Ti. In this work, C coating and C/B$_4$C duplex coating were successfully fabricated onto SiC fibers via chemical vapor deposition (CVD), then consolidated into the SiC$_f$/C/Ti$_2$AlNb and the SiC$_f$/C/B$_4$C/Ti$_2$AlNb composites, respectively, via hot isostatic pressing (HIP) under the condition of 970 °C, 150 MPa, 120 min, and finally furnace cooled to room temperature. The C- and C/B$_4$C-dominated interfacial reactions in the SiC$_f$/C/Ti$_2$AlNb and the SiC$_f$/C/B$_4$C/Ti$_2$AlNb were explored, revealing two different reaction products sequences: The different-sized TiC and the coarse-grained (Ti,Nb)C + AlNb$_3$ for the SiC$_f$/C/Ti$_2$AlNb; and the fine-grained TiB$_2$ + TiC, the needle-shaped (Ti,Nb)B$_2$/NbB + (Ti,Nb)C, the coarse-grained (Ti,Nb)C + AlNb$_2$ for the SiC$_f$/C/B$_4$C/Ti$_2$AlNb. Annealing experiments were further carried out to verify the different reaction kinetics caused by C coating and C/B$_4$C duplex coating. The reaction layer (RL)-dominated interfacial strength and tensile strength estimations showed that higher interface strength and tensile strength occurred in the SiC$_f$/C/Ti$_2$AlNb instead of the SiC$_f$/C/B$_4$C/Ti$_2$AlNb, when the same failure mode of fiber push-out took place.

Keywords: SiC$_f$/Ti$_2$AlNb composite; C coating; C/B$_4$C duplex coating; interfacial reaction; tensile strength

1. Introduction

Continuous SiC fiber-reinforced titanium matrix composites (SiC$_f$/Ti) have been considered as one of most potential light-weight high-strength structural materials required by aerospace vehicles and advanced propulsion system, due to their high specific strength and stiffness at both room and elevated temperature [1–3]. The physical and mechanical properties of several materials for potential applications in the aero-engine field are shown in Table 1 [4]. And the specific strength and stiffness at

room and elevated temperatures of several composites are shown in Figure 1 [5]. Raising the service temperature of SiC_f/Ti is a continuous pursuit driven by many new applications. Recently, intermetallic titanium aluminides (TiAl, Ti_3Al, Ti_2AlNb) have begun to be employed as the matrix of SiC_f/Ti due to their more excellent high temperature performance, as compared with common Ti alloys [6,7]. Among them, Ti_2AlNb alloys with higher ductility and formability have attracted more attention due to their excellent low- and high-temperature loading capabilities [7–10]. Therefore, Ti_2AlNb alloys, especially with O-phase as the main component that contributes a superior ductility [10], would be the potential choice for the development of high-temperature titanium matrix composites (TMCs) [11,12]. Smith et al. fabricated the SCS-6 SiC_f/Ti_2AlNb by foil–fiber–foil processing (FFF) and identified the interfacial products consisting of $TiC_{1-x}+Ti_5Si_3$, $(Ti,Nb,Si)C_{1-x}$, $Al(Ti,Nb)_3C$ and $(Ti,Nb,Al)_5(Si,Al)_3$, with the primary reaction zone size of ~0.6 µm; the SiC_f/Ti_2AlNb exhibited more excellent high temperature performance compared to SiC_f/α_2-Ti and the longitudinal tensile properties of the composite (which are dominated by the fiber strength) were slightly improved due to the orthorhombic matrix. [13]. Luo et al. further introduced C/Mo duplex coatings as barrier layers and prepared the $SiC_f/C/Mo/Ti_2AlNb$ by the FFF method. They found that the Mo barrier layer can regulate the microstructure of the matrix by forming a B_2-riched transition zone between the reaction layer (RL) and the matrix in the SiC_f/Ti-21Al-29Nb composite, obtaining a higher tensile strength relative to the Ti_2AlNb alloy [14]. In addition, Yang et al. employed a matrix-coated fiber (MCF) method to fabricate SCS-6 SiC_f/Ti_2AlNb, and also explored the interfacial reactions between SCS-6 SiC fiber and Ti_2AlNb, showing a milder interfacial reaction than that in $SiC_f/super \alpha_2$-Ti (Ti-25Al-10Nb-3V-1Mo) [15]. Compared with other Ti alloys matrices (Ti-6Al-4V, TC17, IMI834) [5,16,17], Ti_2AlNb acting as the matrix can exactly elevate the service temperature of SiC_f/Ti. However, the SiC_f/Ti_2AlNb is still inadequately understood, especially for the reason that the interfacial reactions of SiC_f/Ti_2AlNb are sensitive to the type of diffusion barrier coating, the microstructure of the matrix, the consolidation process, etc.

Table 1. Comparative properties of Titanium metal matrix composites (Ti MMCs) and superalloys.

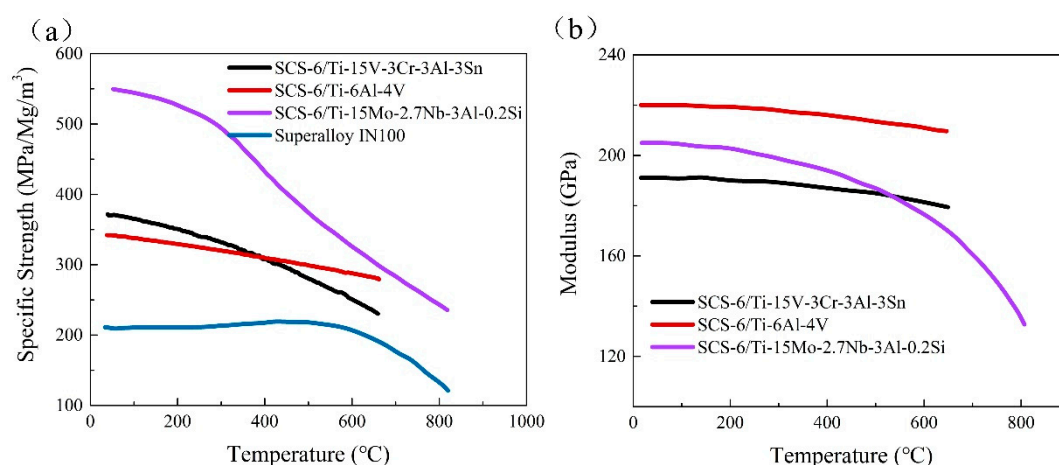| Properties (Direction of Fibers)	Conventional Ti MMC	Ti Aluminide Ti MMC	Superalloys
Density, g/cm^3	4.04	4.18	8.3
Stiffness, GPa	200	242	207
Max use temperature, °C	538	760	1090
CTE, $°C^{-1} \times 10^{-6}$	8.91	9.18	13.0

Figure 1. Specific strength (**a**) and modulus (**b**) of several unidirectional TMCs and a nickel-based superalloy.

It is accepted that the interfacial reactions (mainly including interfacial products and their distribution, and each sub-layer thickness) of SiC_f/Ti would determine the interfacial properties,

and further act on the performances of SiC_f/Ti [2,18]. Accordingly, understanding and further tailoring the interfacial behaviors of SiC_f/Ti_2AlNb would be necessary to ensure its superior properties. Notably, introducing diffusion barrier coatings is still a popular strategy for optimizing the interfacial structure and interfacial properties of SiC_f/Ti, which can not only protect the SiC fiber suffering from the attack from the matrix, but also obtain a moderate interfacial debonding strength arising from the formation of an appropriate interfacial reaction layer. Several potential diffusion barrier coatings, including carbon, carbides, borides, oxides, nitrides, and transition metals, have been investigated to protect SiC fiber and control the interfacial reactions of SiC_f/Ti [19–23]. Among them, C coating is still the most widely used diffusion barrier coatings in the SiC_f/Ti [24,25]. In addition to protecting the SiC fiber, the C coating has the following advantages: (1) It has a good thermal expansion coefficient with SiC fiber; (2) it has a good compatibility with SiC; (3) the interface reaction of composites is easy to control; and (4) the process stability is good. The interfacial reactions between SCS-6 SiC fiber and Ti_2AlNb have been well explored, when the SCS-6 SiC fiber is comprised of surface C coating with some SiC particles in it [15]. However, the interfacial reactions between pure C coating and Ti_2AlNb matrix are still unclear. In addition, Zhang et al. found that as B_4C coating was introduced to SiC_f/TiAl as the diffusion barrier coating, a thin interfacial layer appeared, confirming the role of B_4C coating in serving as a potential barrier coating in the SiC_f/TiAl [26]. Obviously, both C and B_4C are two potential diffusion barrier coatings in the SiC_f/Ti_2AlNb. A comparative study on the interfacial reactions of SiC_f/Ti_2AlNb with C and B_4C diffusion barrier coatings would; thus, be helpful to understand their interfacial behaviors.

In the present paper, C coating and C/B_4C duplex coatings were, respectively, prepared on SiC fibers by chemical vapor deposition (CVD) as different diffusion barrier layers, Then two kinds of SiC_f/C/Ti_2AlNb and SiC_f/C/B_4C/Ti_2AlNb composites were successfully fabricated by MCF method and hot isostatic pressing (HIP) consolidation. Finally, C and C/B_4C diffusion barrier layer-dominated interfacial reactions, matrix microstructure evolutions, interfacial debonding strength, and tensile strength were investigated.

2. Materials and Methods

2.1. Sample Preparation

C-coated and C/B_4C-coated SiC fibers about 100 μm in diameter (provided by AECC Beijing Institute of Aeronautical Materials, Beijing, China) were prepared by CVD. MCF method was employed to fabricate Ti_2AlNb coatings onto tungsten-cored SiC monofilament as precursor wires in a facing-targets magnetron-sputtering system, with the Ti_2AlNb alloy (nominal composition in at.% of Ti-22Al-25Nb) utilized as targets and the coated SiC fibers used as substrates. Next, these precursor wires were put into a Ti_2AlNb alloy canister hermetically, which was then sealed using electron beam welding. Subsequently, the SiC_f/Ti_2AlNb was manufactured by consolidating those packed precursor wires through HIP under the soaking temperature, pressure, holding-time conditions of 970 °C, 150 MPa, 120 min, respectively, and then furnace cooled to the room temperature. This group of HIP process parameters is based on previous research [27]. With this process employed, the composite material can be completely closed, the diffusion barrier coating remains unfailing, and the RL will not be too intense. Clearly, after HIP, two composites evolving from C-coated and C/B_4C-coated SiC fibers were named as SiC_f/C/Ti_2AlNb and SiC_f/C/B_4C/Ti_2AlNb, respectively.

2.2. Characterization

The sectional morphology and chemical binding state of C and C/B_4C coatings on SiC fibers were analyzed respectively by scanning electron microscope (SEM, FEI nano 450, Hillsboro, OR, USA), as well as ESCALAB-250 X-ray photoelectron spectrum (XPS, Waltham, MA, USA) using Al Ka radiation as the X-ray source with an energy of 1 keV. The consolidated composite specimens designated for microstructural observation by SEM were cut along the cross-section, polished, and

etched in a 10% HF + 30% HNO_3 solution. Specimens for transmission electron microscope (TEM) observation were cut from the composites in two directions, perpendicular to the cross-section and in the radial direction of the fiber, by FEI Quanta 200 FEG focused ion beam milling (FIB, Hillsboro, OR, USA) [28]. The interfacial reaction products were investigated by field emission JEOL 2010F TEM (Tokyo, Japan,) and the chemical compositions of the sub-layer in interfacial zones were further examined by energy-dispersive X-ray spectrometer (EDS) equipped in TEM. In order to study the kinetics of interfacial reaction, the composite samples were heat treated in vacuum at 800, 850, 900, and 950 °C for 36, 64, 100, 144, and 196 h, respectively. The total thickness of RL for these heat treatment samples was measured by SEM. Nanoindenter (Nano Test Xtreme, Micro Materials, Wrexham, UK) was employed to evaluate the interfacial debonding strength via fiber push-out test with the sample slices with 0.35 ± 0.01 mm thickness [29]. Two tensile samples were prepared for each HIP consolidated specimen with the gauge dimensions of $\Phi 3 \times M6$, as shown in Figure 2, and the composite material inside the tensile specimen was ~2.8 mm in diameter. The room temperature tensile tests were performed at an extension rate of 1 mm/min, using the Inspekt Table 100 kN model universal testing machine. The fractographies were observed by SEM and laser scanning confocal microscope (LSCM, KEYENCE VK-100, Osaka, Japan).
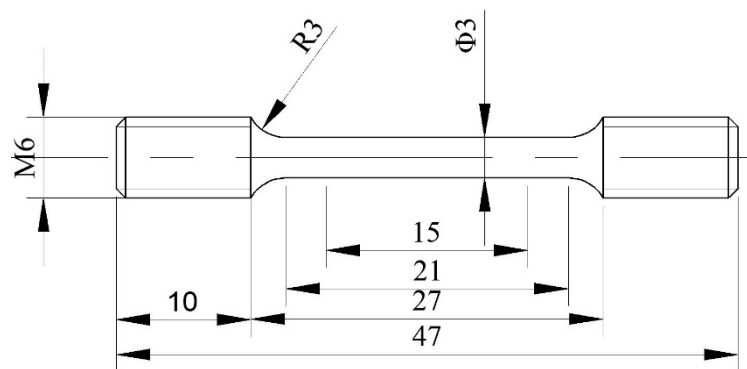

Figure 2. Tensile specimens of SiC_f/Ti_2AlNb.

3. Results and Discussion

3.1. Microstructure of C and C/B$_4$C Coatings

As expected, C coating and C/B$_4$C duplex coating were successfully fabricated on SiC fibers by CVD. The results of SEM (Figure 3a,b) reveal that the uniform-thickness C single coating and the C/B$_4$C duplex coating can be clearly identified and were located between SiC fibers and Ti_2AlNb matrix coatings. It is noted that the thickness of C single coating was ~1.5 μm, which was almost the same as the C layer-thickness in the C/B$_4$C duplex coating, and the total thickness of the C/B$_4$C duplex coating approached ~3.5 μm. The ~20 μm thickness Ti_2AlNb coatings on both barrier coatings are clearly visible, which were deposited by PVD process and would evolve into the matrix during consolidation. The morphologies of the two composites after consolidation are shown in Figure 4. XPS was further used to investigate the chemical binding of the C and B$_4$C coatings. For C coating, the XPS C 1s spectrum is presented in Figure 3c, which could be deconvoluted into two peaks located at ~284.5 and ~285.0 eV, corresponding to sp^2-hybridized and sp^3-hybridized carbon, respectively. As suggested by the following high-resolution TEM (HRTEM) in Figure 5i, the C coating was a typical pyrolytic carbon exhibiting a turbostratic carbon structure in nature. This structure consists of small basic structural units (BSUs) mainly comprising nanoscale few-layer graphene planes. Thus, the sp^2-hybridized carbon should come from graphene planes in BSUs of the C coating [16]. In contrast, the sp^3 peak should be assigned to defects in graphene planes or the amorphous region in pyrolytic carbon due to its nature of high-density defects [30,31]. The integral area ratio of sp^2 and $sp^2 + sp^3$ was calculated to be 76.0%, which suggested that the C coating exists mainly in the form of sp^2-hybridized graphene planes in

BSUs and still possess high-density defects in graphene planes. For B_4C coating, the XPS B 1s spectrum is shown in Figure 3d, and the deconvolution revealed the existence of two boron chemical states at the binding energies of 187.7 and 188.8 eV, corresponding to the B–B and B–C bonds, respectively [32]. This suggests that the B_4C coating still possesses a large amount of B–B bonds.
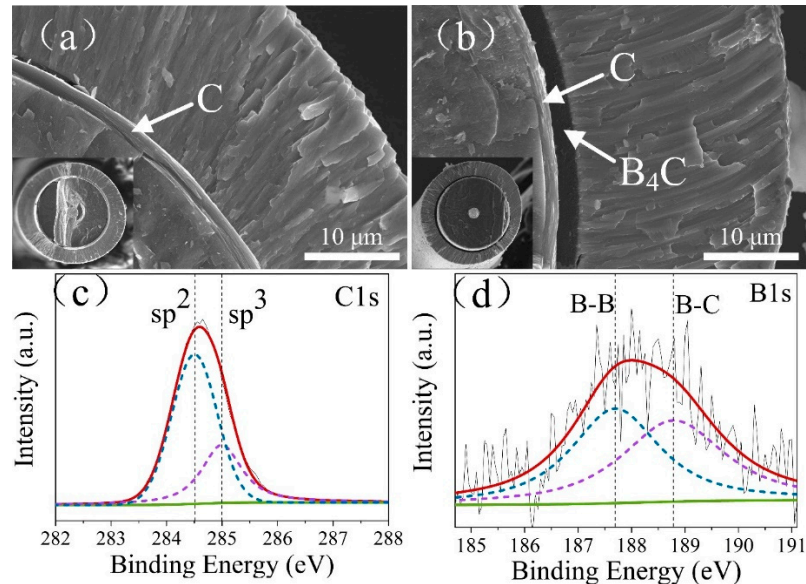

Figure 3. Cross-sectional SEM micrographs of SiC_f/Ti_2AlNb precursor wires for (**a**) $SiC_f/C/Ti_2AlNb$ and (**b**) $SiC_f/C/B_4C/Ti_2AlNb$; and typical XPS patterns for (**c**) C coating and (**d**) B_4C coating.
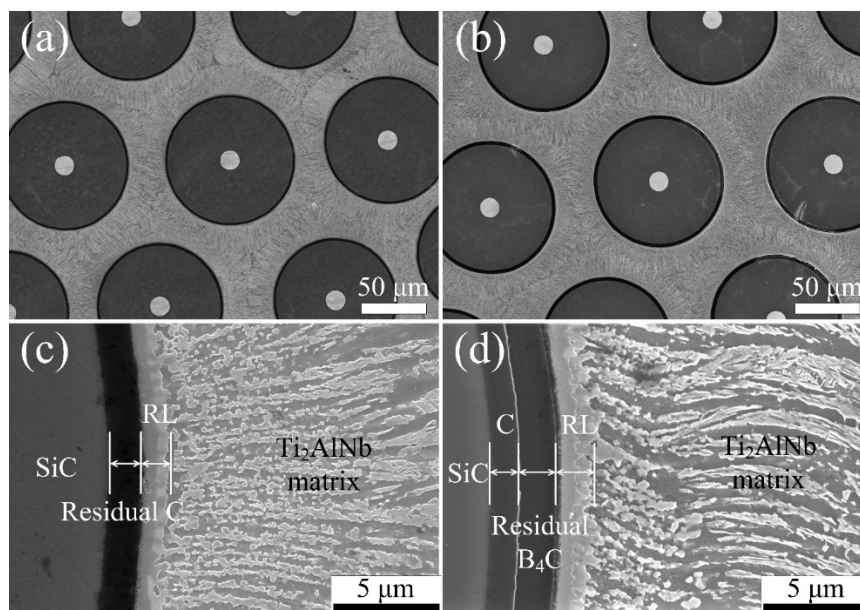
Figure 4. Microstructure of SiC_f/Ti_2AlNb observed by SEM for (**a,c**) $SiC_f/C/Ti_2AlNb$ and (**b,d**) $SiC_f/C/B_4C/Ti_2AlNb$.

HRTEM and selected-area electron diffraction (SAED) were further used to analyze the microstructure of C and B_4C coatings, which are shown in Figure 5i and Figure 6i, respectively. It reveals that C coatings exhibited a typical turbostratic carbon structure with a certain degree of tortuosity in lattice fringes, in which BSUs contained seven to eight layers (d space: 0.368 nm) as marked in the HRTEM. According to the model proposed by Reznik et al., the SAED patterns further suggested the formation of high-texture carbon by the appearance of orientation angle (OA) of 47° [33,34]. In contrast, the B_4C

coating exhibited a typical polycrystalline structure with the random B_4C nano-particles (~10 nm in average grain size) surrounded by a small amount of amorphous phases, as revealed by the HRTEM images and corresponding SAED in Figure 6i.
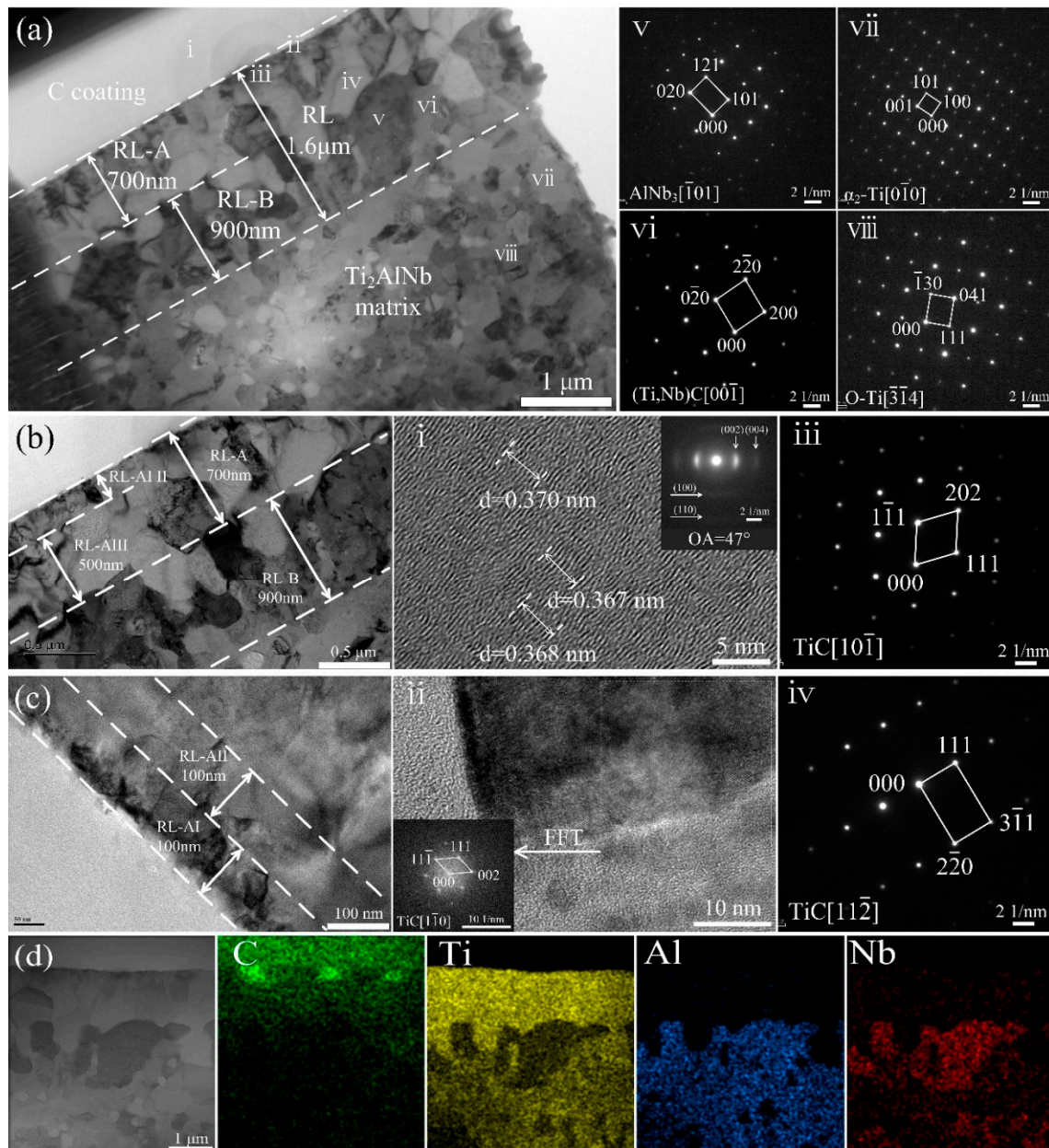

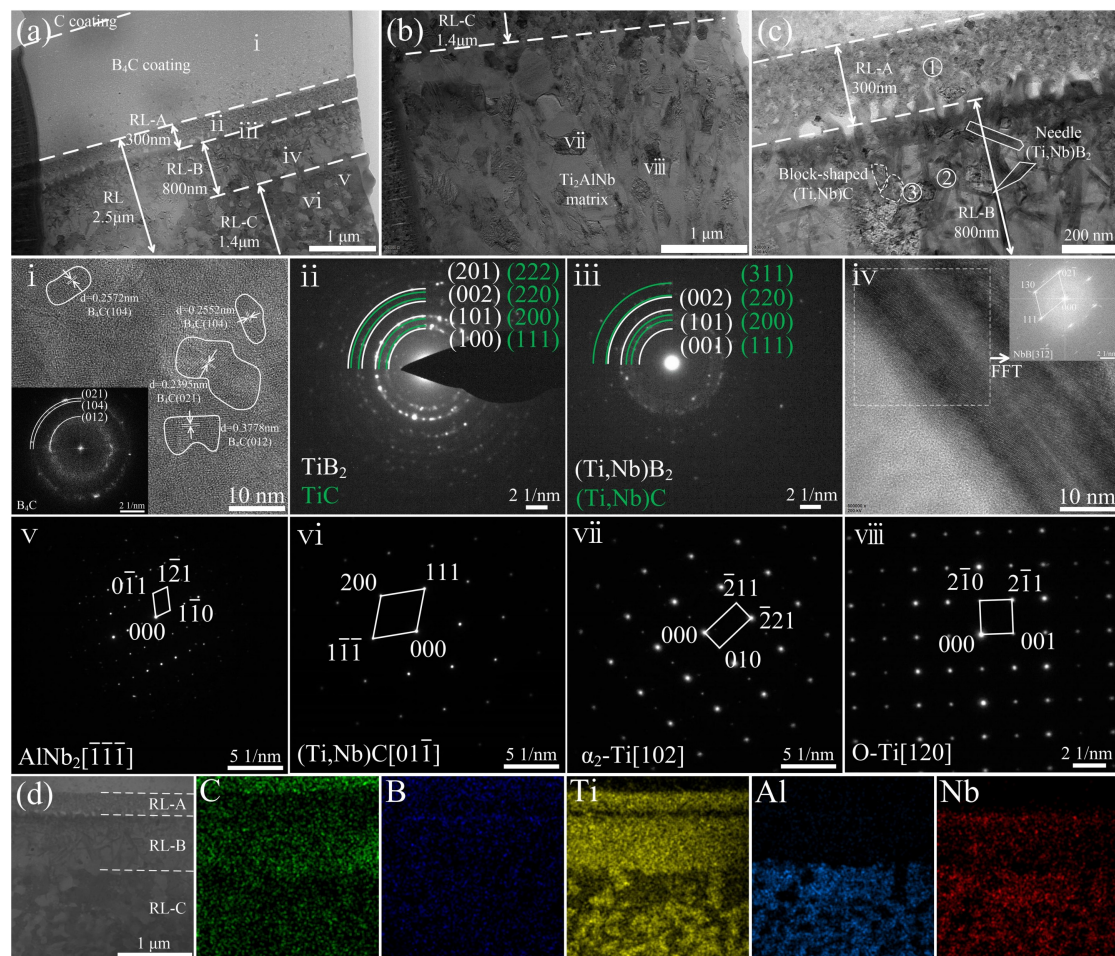**Figure 5.** (**a–c**) TEM bright field images and high magnification images of interfacial reaction products for $SiC_f/C/Ti_2AlNb$; (**d**) STEM image and EDS mappings of the interfacial zones for $SiC_f/C/Ti_2AlNb$; (**i–viii**) shows the HRTEM images of C coating and SAED patterns of interfacial reaction products for $SiC_f/C/Ti_2AlNb$ marked in (a).

Figure 6. (**a–c**) TEM bright field images and high magnification images of interfacial reaction products for SiC$_f$/C/B$_4$C/Ti$_2$AlNb; (**d**) STEM image and EDS mappings of the interfacial zones for SiC$_f$/C/B$_4$C/Ti$_2$AlNb; (**i–viii**) shows the HRTEM images of B$_4$C coating and SAED patterns of interfacial reaction products for SiC$_f$/C/B$_4$C/Ti$_2$AlNb marked in (a) and (b).

3.2. Interfacial Reactions in the SiC$_f$/C/Ti$_2$AlNb and SiC$_f$/C/B$_4$C/Ti$_2$AlNb

Figure 4a,b show the cross-sectional overview of the SiC$_f$/C/Ti$_2$AlNb and SiC$_f$/C/B$_4$C/Ti$_2$AlNb after consolidating at the same HIP condition. The fibers in both composites were uniformly arranged in a hexagonal distribution. Apparently, the interfacial reaction layers could be found between the residual barrier layer and the Ti$_2$AlNb matrix in both composites, which might mainly come from the interdiffusion of elements between the adjacent layers during high-temperature HIP consolidation [2]. In the SiC$_f$/C/Ti$_2$AlNb, the RL was compact with no cracks or holes, and its thickness was evaluated to be ~1.6 μm. As C coating was utilized as the barrier layer of SiC$_f$/Ti, the RL mainly arose from the continuous diffusion of C atoms from C coating into the adjacent Ti matrix and was essentially a TiC-based RL [16]. Near the RL, the Ti$_2$AlNb matrix showed in a typical block or strip morphology. In the SiC$_f$/C/B$_4$C/Ti$_2$AlNb, a thicker RL of ~2.5 μm in thickness formed between the B$_4$C and Ti$_2$AlNb matrix, as compared with that in the SiC$_f$/C/Ti$_2$AlNb. Compared to the SiC$_f$/C/Ti$_2$AlNb, the SiC$_f$/C/B$_4$C/Ti$_2$AlNb allowed the boron atoms with a smaller size to easily diffuse in the gaps and the grain boundaries at a higher rate, consequently forming a thicker interfacial reaction layer. Clearly, besides the thickness of RL, the reaction products and their distribution in the RL can strongly impact on interfacial properties. In order to clarify the products distribution and the diffusion barriers-dominated interfacial reaction, the interfacial reaction zones were further observed by TEM

TEM bright field images of the interfacial reaction zones and the Ti$_2$AlNb matrix in the SiC$_f$/C/Ti$_2$AlNb are shown in Figure 5. EDS analyses on concerned points are shown in Table 2.

Based on the reaction products, the RL could be divided into two sub-layers, namely, RL-A near C coating and RL-B adjacent to the Ti_2AlNb matrix. The RL-A was composed of TiC_x, while the RL-B consisted of $(Ti,Nb)C+AlNb_3$, as identified by the HRTEM and the SAED patterns in Figure 6ii–vi. Enlarged images of the RL-A are also displayed in Figure 5b,c. On basis of the size of TiC_x grains, the RL-A could be further divided into RL-AI (fine-grained TiC_x layer adjacent to C coating), RL-AII (transition layer of TiC_x in the middle of RL-A zone), and RL-AIII (coarse-grained TiC_x layer next to the RL-B). For $SiC_f/C/Ti_2AlNb$, the total thickness of RL-A was evaluated to be ~0.7 μm, consisting of ~100 nm RL-AI, ~100 nm RL-AII, and ~0.5 μm RL-AIII. Meanwhile, the grain size considerably increased from less than 100 nm for RL-AI to ~200 nm for RL-AII and ~500 nm for RL-AIII The gradual increase in TiC_x grain size along RL-A could be explained by the fact that C atoms continuously diffuse from the C coating toward the matrix and the matrix grains grow at the same time during HIP. A description for the process of RL formation is available in our previous paper [28]. Unlike the RL-A that was only composed of TiC_x, the RL-B mainly comprised $(Ti,Nb)C$ and $AlNb_3$, as confirmed by SAED and EDS in Figure 5v,vi. The scanning TEM (STEM) images and EDS mapping analyses of elements were obtained to further visualize the elemental distribution of the interfacial zones of the $SiC_f/C/Ti_2AlNb$, as shown in Figure 5d. The metallic elements in the matrix were almost completely blocked and located outside the C coating. By contrast, C atoms diffused from the C coating toward the matrix, which dominated the formation of interfacial reaction zones with C content gradient. Obviously, the reaction products in RL-A were all TiC. Based on the above observations, the sequence of reaction products in $SiC_f/C/Ti_2AlNb$ was TiC and $(Ti,Nb)C+AlNb_3$. This can be discussed as follows. Compared with the FFF foils commonly used by many researchers, the PVD Ti_2AlNb was composed of lots of nanocrystalline grains, which could provide a large amount of channels for elemental diffusion. Accordingly, the interfacial reaction was supposed to be a reaction- and diffusion-controlled process. Table 3 lists the equations for describing the possible interfacial reactions occurring in the $SiC_f/C/Ti_2AlNb$ composites and the corresponding ΔrG values [35,36]. Reaction 5 has a more negative value of ΔrG than reaction 10. In addition, Ti atoms have a higher diffusion rate than Nb atoms to the C coating during the reaction [37]. They resulted in the formation of TiC in the initial stage of the reaction. At the same time, the remaining high concentration of Al and Nb elements in the Ti-depletion matrix formed $AlNb_3$. During the reaction, the elemental diffusion occurred simultaneously with the grain growth. When the near-stoichiometric TiC formed and thus became a C-diffusion barrier, the interfacial reaction that followed would transit from the reaction-controlled to the diffusion-controlled. Since the C source was absolutely sufficient, only a small amount of C passed through the RL-A and was located at its front end, and reacted with the Ti and Nb in the matrix to form $(Ti,Nb)C$. In this process, the formation of the relatively-stable $AlNb_3$ phase and $(Ti,Nb)C$ resulted in an Al-enriched zone, in which the reaction with C did not occur, thereby increasing the transition temperature of B_2 phase in Ti_2AlNb matrix. Near RL-B, the Ti_2AlNb matrix mainly consisted of α_2 and O phases, as identified by SAED.

Table 2. Chemical composition of interfacial reaction products in $SiC_f/C/Ti_2AlNb$ composite (at.%).

Position	C	Ti	Al	Nb
a (ii)	80.15	19.85	-	-
a (iv)	76.54	23.46	-	-
a (v)	17.23	16.29	18.63	47.85
a (vi)	59.75	33.85	0.40	6.00

Table 3. Equations of the interfacial reactions occurred in $SiC_f/C/Ti_2AlNb$ and $SiC_f/C/B_4C/Ti_2AlNb$ composites and the corresponding ΔrG values at 970 °C.

No.	Interfacial Reaction Equation	ΔrG/kJ mol^{-1}
1	$2Ti + B_4C = 2TiB_2 + C$	−230.5
2	$Ti + 2B = TiB_2$	−258.7
3	$Ti + B = TiB$	−155.6
4	$Ti + B_4C = TiC + 4B$	−111.9
5	$Ti + C = TiC$	−170.3
6	$TiB_2 + Ti = 2TiB$	−52.4
7	$2Nb + B_4C = 2NbB_2 + C$	−133.7
8	$Nb + 2B = NbB_2$	−162.9
9	$Nb + B = NbB$	−107.7
10	$Nb + C = NbC$	−134
11	$4Al + 3C = Al_4C_3$	−138

TEM bright field images and EDS analyses of the interfacial reaction zones in the $SiC_f/C/B_4C/Ti_2AlNb$ are shown in Figure 6a,b and Table 4, respectively. The RLs (~2.5 μm in total thickness) could be divided into three sublayers based on the reaction products, namely RL-A, RL-B, and RL-C. Enlarged images of the RL-A and the RL-B are also displayed in Figure 6c. The RL-A, adjacent to the B_4C coating, was composed of fine-grained TiB_2 and TiC with the grain size of ~20 nm, as revealed by the SAED patterns in Figure 6ii. This means that only Ti reacted with B and C in the RL-A. Across the RL-A, both Ti and Nb reacted with B and C, forming the RL-B. Thus, the RL-B consisted mainly of the block-shaped (Ti,Nb)C and the needle-shaped $(Ti,Nb)B_2$ with the elongated grains, as indicated by SAED and EDS in Figure 6iii,iv and Table 2. Unlike the carbide products with equiaxed feature, the boride products existed in needle shape when their composition deviated from the stoichiometry [15]. In the RL-C outside the RL-B, only the C atom diffused across RL-B, whereas the B atom diffusion terminated in RL-B, forming the coarse-grained (Ti,Nb)C with the grain size of ~100 nm, together with $AlNb_2$, as revealed by SAED and EDS in Figure 6v,vi. Figure 6d shows the STEM images and EDS elemental maps of the interfacial zones in the $SiC_f/C/B_4C/Ti_2AlNb$ for further visualizing the elemental distribution. All reactions occurred outside the B_4C coating, and the diffusion of B and C atoms dispersedly distributed throughout the reaction zone and dominated the reactants. The Ti, Nb, and Al elements started to appear in RL-A, RL-B, and RL-C in turn due to their different reactivity. Additionally, the clear boundaries of B_4C coating and each sublayer of interfacial reaction zones can be distinguished in the $SiC_f/C/B_4C/Ti_2AlNb$. The sequence of reaction products in the $SiC_f/C/B_4C/Ti_2AlNb$ was TiB_2+TiC, $(Ti,Nb)B_2+(Ti,Nb)C+NbB$, and $(Ti,Nb)C+AlNb_2$, and will be discussed in detail as follows.

Table 4. Chemical composition of interfacial reaction products in $SiC_f/C/B_4C/Ti_2AlNb$ composite (at.%).

Position	B	C	Ti	Al	Nb
Spot 1 (RL-A)	65.14	14.10	20.76	-	-
Spot 2 (fine needle in RL-B)	62.25	9.50	13.88	0.23	14.13
Spot 3 (block in RL-B)	40.21	28.27	27.38	0.23	3.91

RL—reaction layer, The RLs could be divided into three sublayers based on the reaction products, namely RL-A, RL-B, and RL-C.

The initial stage of the interfacial reaction was a reaction-controlled process. The reactions (1), (2), (5), and (3), as listed in Table 3, took place preferentially because of the high diffusion rate of Ti and the high absolute values of ΔrG, and resulted in the production of TiB_2 and TiC near the B-rich B_4C coating in the RL-A. High concentration of B-rich B_4C contributed to the production with high nucleation rate that hindered the grain growth of TiB_2 and TiC, and lots of fine grains provided terrible crystalline-boundary diffusion paths for B and C atoms in the RL-A. As the reaction and the diffusion of the elements proceeded synchronously, Nb atoms began to participate during the

reaction. A large amount of near-stoichiometric boride and (Ti,Nb)C (Ti-rich) in needle and block shape, respectively, were formed in the RL-B. These products in RL-B could be regarded as the diffusion barrier layer, which led to the interfacial reaction entering the diffusion-controlled dominated stage. After the formation of previous products, the remnant highly-concentrated elements of Nb and Al in the Ti-depletion matrix formed $AlNb_2$ in the RL-C. Compared with the $AlNb_3$ formation in the RL-B of $SiC_f/C/Ti_2AlNb$, the $AlNb_2$ formation could be attributed to a certain amount of participated Nb atoms during the preformation of the borides. Simultaneously, a small amount of carbon released by the reactions diffused into the matrix and formed a bit of (Ti,Nb)C. Due to the equilibrium of reaction process, a large amount of Al atoms were not involved in the reactions, leading to the Al-enriched matrix. Consequently, the main constituent phases of this matrix adjacent to the RL-C were α_2-Ti and O-Ti. The sequence of reaction products in the $SiC_f/C/B_4C/Ti_2AlNb$ is accordingly summarized in the schematic diagram, as shown in Figure 7.
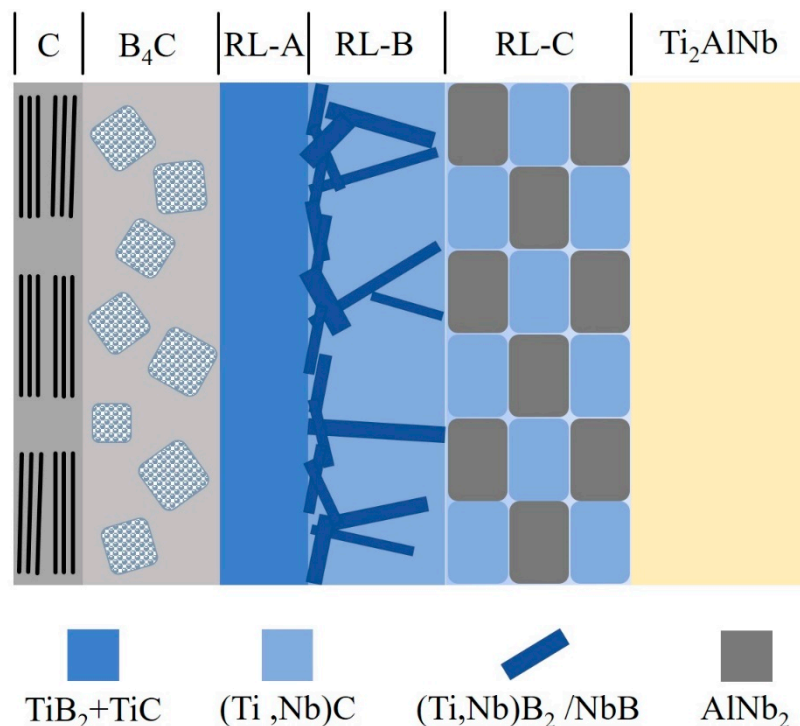
Figure 7. Schematic of interfacial reaction products in $SiC_f/C/B_4C/Ti_2AlNb$ composite.

In summary, the comprehensive SEM and TEM observations make it clear that in both the $SiC_f/C/Ti_2AlNb$ and the $SiC_f/C/B_4C/Ti_2AlNb$ composites, the RL zones were formed via a two-stage process: the reaction-controlled and the diffusion-controlled. The according reaction products were identified as the different-sized TiC and the coarse-grained $(Ti,Nb)C+AlNb_3$ for the $SiC_f/C/Ti_2AlNb$, and the fine-grained TiB_2+TiC, the needle-shaped $(Ti,Nb)B_2/NbB+(Ti,Nb)C$ and the coarse-grained $(Ti,Nb)C+AlNb_2$ for the $SiC_f/C/B_4C/Ti_2AlNb$. Compared with the C single coating, owing to the B_4C acting as the reaction front in the C/B_4C duplex coating, the needle-shaped boride products facilitated elements diffusion and; thereby, formed a thicker RL.

3.3. Reaction Kinetics of $SiC_f/C/Ti_2AlNb$ and $SiC_f/C/B_4C/Ti_2AlNb$

The interfacial reaction kinetics of SiC_f/Ti is normally an indispensable and important basis for evaluating the thermal stability of SiC_f/Ti and understanding the interfacial reaction mechanism of SiC_f/Ti. The thickness of interfacial reaction zone develops progressively with the thermal exposure temperature and the increase of time. In detail, the thickness of RL is linearly related to the square of heat treatment time for the interfacial reaction zone in which the diffusion-controlled process

dominates [38]. The total thickness of RL plotted as a function of the square root of reaction times at various heat treatment temperatures for the $SiC_f/C/Ti_2AlNb$ and the $SiC_f/C/B_4C/Ti_2AlNb$ composites was estimated, respectively, and is shown in Figure 8a,b.
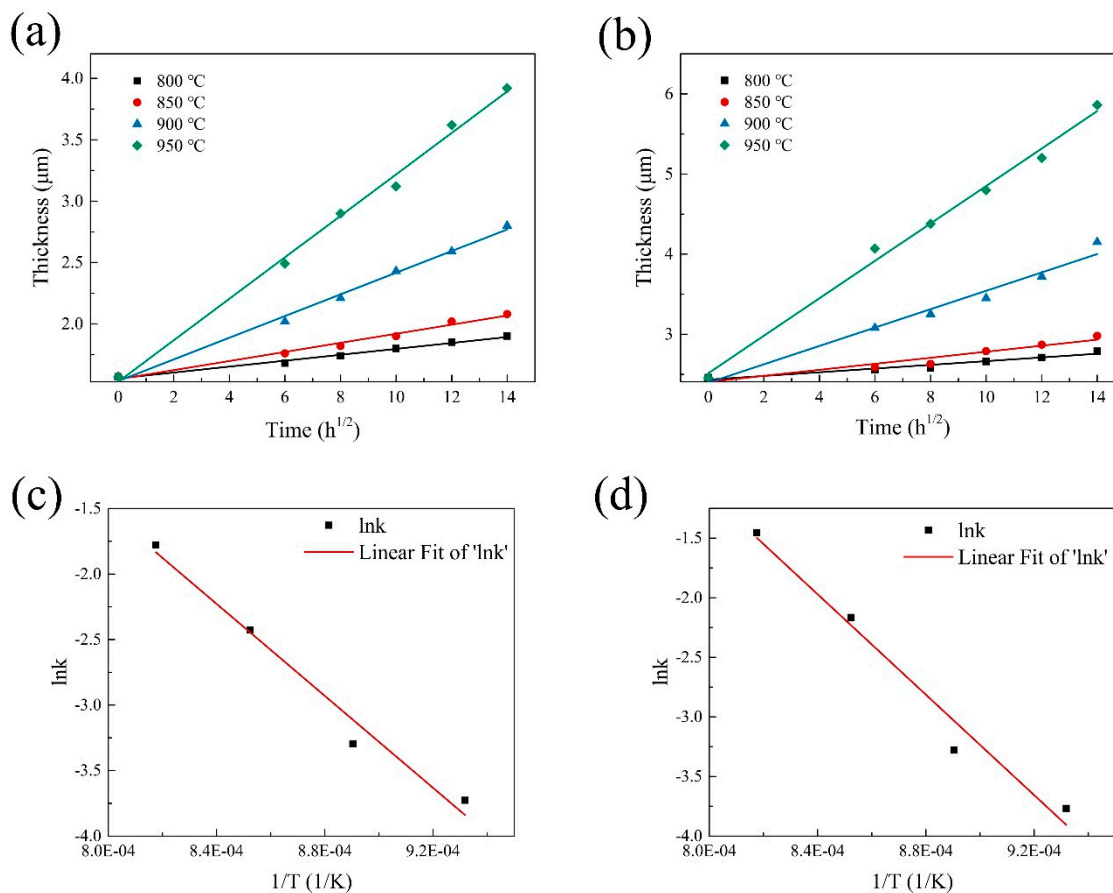

Figure 8. The total thickness of the reaction zone at various temperatures as a function of the square root of time for (**a**) $SiC_f/C/Ti_2AlNb$ and (**b**) $SiC_f/C/B_4C/Ti_2AlNb$ composites; the logarithm of the reaction rates vs. reciprocal of the heat treatment temperature for (**c**) $SiC_f/C/Ti_2AlNb$ and (**d**) $SiC_f/C/B_4C/Ti_2AlNb$ composites.

The reaction kinetics can be described by the following equations [39]:

$$x = kt^{1/2} + b_0, \tag{1}$$

$$k = k_0 exp(-Q/2RT) \tag{2}$$

where x is the thickness of the RL, t is time, k is the reaction rate constant, b_0 is the original thickness of the RL, R is the gas constant, Q is the activation energy, k_0 is the frequency factor, and T is the temperature. The reaction rate k was determined from the slope of the curves for fitting the thickness of RL at different times. The logarithm of k vs. the reciprocal of T, according to Equation (2), was plotted and is shown in Figure 8c,d. The Q and k_0 of the interfacial chemical reactions were subsequently calculated.

The activation energy Q and the rate constant k_0 for the $SiC_f/C/Ti_2AlNb$ and $SiC_f/C/B_4C/Ti_2AlNb$ composites were 292 kJ/mol, 0.457 cm/s$^{1/2}$ and 350 kJ/mol, 11.4 cm/s$^{1/2}$, respectively. Both the Q and the k_0 can normally affect the growth of the RL in SiC_f/Ti. The Q of $SiC_f/C/B_4C/Ti_2AlNb$ was larger than that of $SiC_f/C/Ti_2AlNb$, indicating that the former would be more difficult to react in the early reaction-controlled stage. However, since the pyrolytic C coating with stronger texture could hinder the outward diffusion of C atoms and the needle-shaped borides could facilitate the elemental diffusion, the k_0 of $SiC_f/C/B_4C/Ti_2AlNb$ was much higher than that of $SiC_f/C/Ti_2AlNb$, which thereby resulted in

a thicker RL of the former under the same consolidating conditions. Therefore, the growth rate of the RL in SiC_f/Ti_2AlNb is dependent on the interaction between the Q and the k_0.

3.4. Interfacial Strength and Tensile Strength

The effect of RL thickness and reaction products on the SiC_f/Ti composites were further explored by mechanical properties tests. It has been widely accepted that the interface strength of SiC_f/Ti is a crucial parameter governing the failure modes of composites subjected to an external load, and thereby plays an important role in controlling the overall mechanical properties. Thus, push-out experiments were carried out to evaluate the interfacial properties of $SiC_f/C/Ti_2AlNb$ and $SiC_f/C/B_4C/Ti_2AlNb$ composites. The load vs. displacement curve was determined and is shown in Figure 9. The interphase shear strength or interface strength, τ_d, at the load level, P_d, corresponding to the initial debonding, can be calculated based on the following formula [40]:

$$\tau_d = P_d/\pi d_f h \tag{3}$$

where d_f is the diameter of SiC fiber and h is the thickness of composite. The average values of P_d for $SiC_f/C/Ti_2AlNb$ and $SiC_f/C/B_4C/Ti_2AlNb$ were measured to be ~7.9 and ~5.6 N, respectively. By substituting P_d, the calculated values of τ_d were ~72 MPa for $SiC_f/C/Ti_2AlNb$ and ~51 MPa for $SiC_f/C/B_4C/Ti_2AlNb$. Fibers push-out were verified through SEM observations of the front and the reverse side of each specimen, as shown in Figure 10. The interfacial debonding took place at the location between the C coating and the RL for the $SiC_f/C/Ti_2AlNb$, and at the location between the C coating and the B_4C coating for the $SiC_f/C/B_4C/Ti_2AlNb$. It is generally believed that, within a certain thickness range, the τ_d of the composites can be determined by the thickness of interfacial zone including diffusion barriers and RL. An elevated thickness of the interfacial zone appropriately would result in a higher value of τ_d for $SiC_f/C/Ti_2AlNb$ [16,27,28]. However, the interfacial debonding that occurred between pyrolytic carbon and amorphous polycrystalline structure of B_4C resulted in a poor interfacial bond strength. Therefore, the τ_d for $SiC_f/C/B_4C/Ti_2AlNb$ was lower than that for $SiC_f/C/Ti_2AlNb$, even though the former had a thicker interfacial zone.
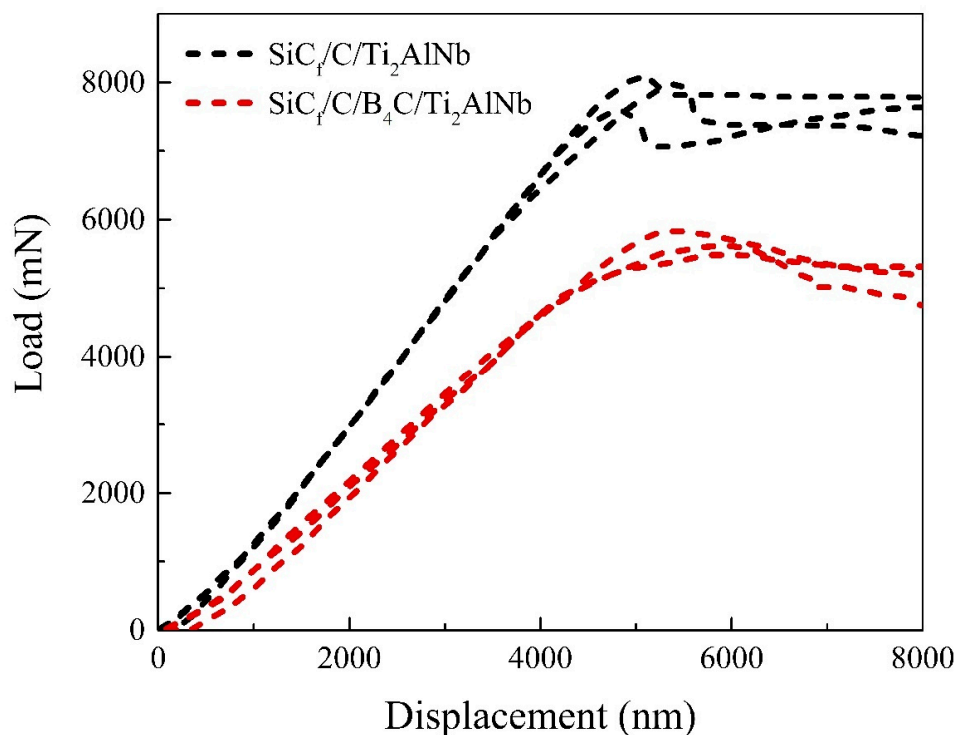

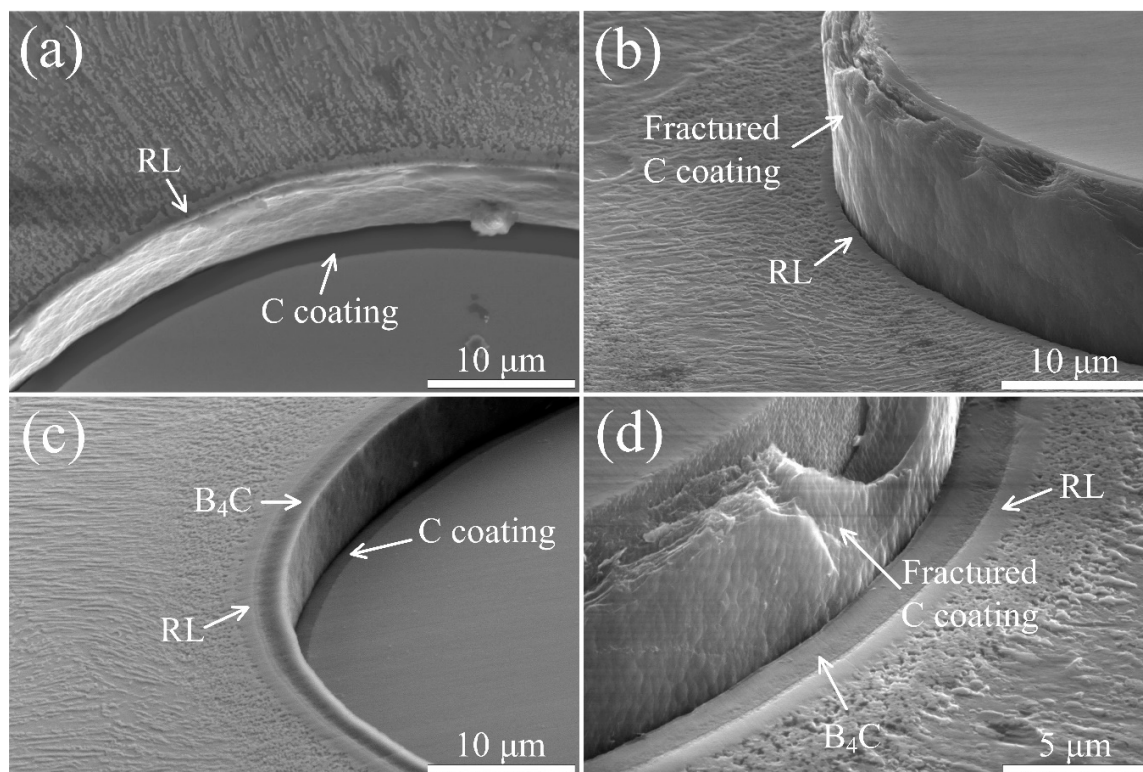**Figure 9.** Typical fiber push-out load–displacement curves for $SiC_f/C/Ti_2AlNb$ and $SiC_f/C/B_4C/Ti_2AlNb$.

Figure 10. Appearance of the push-out fibers at the top and bottom of the test specimen for (**a,b**) SiC$_f$/C/Ti$_2$AlNb and (**c,d**) SiC$_f$/C/B$_4$C/Ti$_2$AlNb.

We further carried out the room temperature tensile tests of the SiC$_f$/C/Ti$_2$AlNb and the SiC$_f$/C/B$_4$C/Ti$_2$AlNb composites, with the tensile curves of SiC$_f$/C/Ti$_2$AlNb and SiC$_f$/C/B$_4$C/Ti$_2$AlNb shown in Figure 11. The average tensile strength values of SiC$_f$/C/Ti$_2$AlNb and SiC$_f$/C/B$_4$C/Ti$_2$AlNb were calculated to be ~1360 and ~1150 MPa, respectively. The tensile strength of SiC$_f$/C/Ti$_2$AlNb is ~200 MPa higher than that of SiC$_f$/C/B$_4$C/Ti$_2$AlNb. This could be attributed to the difference in interfacial zone, although they had the same fibers and matrix alloy. Figure 12 shows the tensile fracture morphologies of SiC$_f$/C/Ti$_2$AlNb and SiC$_f$/C/B$_4$C/Ti$_2$AlNb. Both two composites displayed an identical step-like fracture mode. This fracture behavior involved only the obvious push-out of short fibers; not the brush-like fracture caused by a too-low τ_d nor the brittle facture induced by a too-high τ_d due to lower interfacial debonding. However, in contrast to the fractograph of SiC$_f$/C/B$_4$C/Ti$_2$AlNb, the fractograph of SiC$_f$/C/Ti$_2$AlNb exhibited more serious steps between the near regions of fiber and the surrounding matrix, corresponding to more obvious crack deflections. The difference in fracture characteristics are determined by the τ_d. Compared with the SiC$_f$/C/B$_4$C/Ti$_2$AlNb, more cracks usually initiated at the interfacial layers of the SiC$_f$/C/Ti$_2$AlNb, that has a higher τ_d and better interface/matrix matching, as the process of continuous loading increased. When the crack passing through the brittle Ti$_2$AlNb matrix propagated to the next interfacial layer, the crack easily changed the propagation direction and continued to extend along the plane of other cracks. This fracture behavior means that the crack would travel through a longer path and consume more fracture energy. Probably for this reason, the SiC$_f$/C/Ti$_2$AlNb had a higher tensile strength than the SiC$_f$/C/B$_4$C/Ti$_2$AlNb, with more fiber bridges in the fracture morphology of SiC$_f$/C/Ti$_2$AlNb, as shown in Figure 12a. In a word, as the interfacial debonding totally dominated the tensile failure, the higher τ_d would aid in improving the tensile strength.
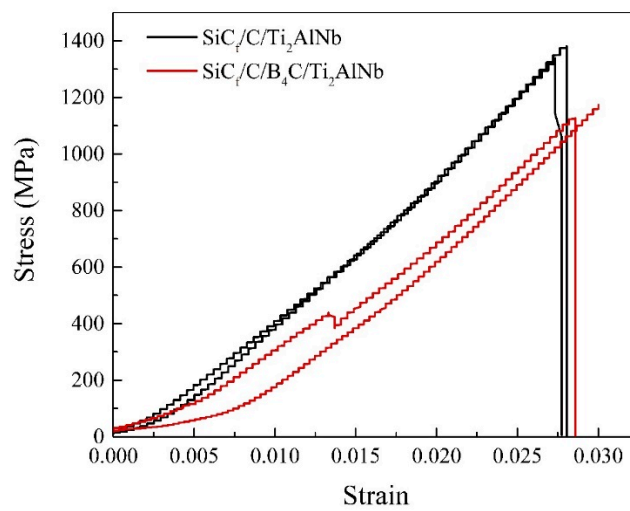
Figure 11. Typical tensile stress–strain curves of SiC$_f$/C/Ti$_2$AlNb and SiC$_f$/C/B$_4$C/Ti$_2$AlNb.
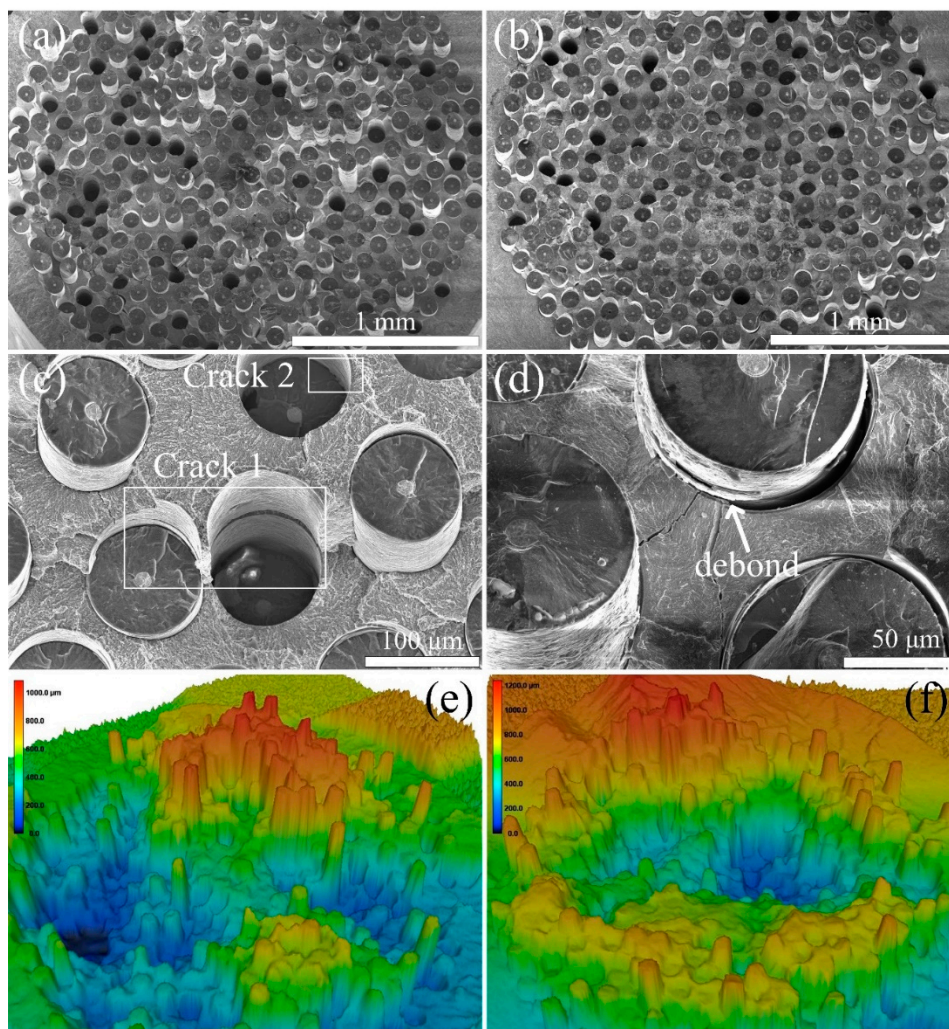
Figure 12. Low-magnification fractographs of (**a**) SiC$_f$/C/Ti$_2$AlNb and (**b**) SiC$_f$/C/B$_4$C/Ti$_2$AlNb; high-magnification fractographs of (**c**) SiC$_f$/C/Ti$_2$AlNb and (**d**) SiC$_f$/C/B$_4$C/Ti$_2$AlNb; fracture morphologies of (**e**) SiC$_f$/C/Ti$_2$AlNb and (**f**) SiC$_f$/C/B$_4$C/Ti$_2$AlNb observed by LSCM.

4. Conclusions

Both C coating and C/B$_4$C duplex coating were successfully fabricated onto SiC fibers by CVD and then consolidated into SiC$_f$/C/Ti$_2$AlNb and SiC$_f$/C/B$_4$C/Ti$_2$AlNb after HIP. On the basis of microstructure observations and mechanical properties tests of two composites, we make the following conclusions:

(1) C-coated and C/B$_4$C duplex-coated SiC fiber-reinforced Ti$_2$AlNb composites were fabricated and the interfacial reaction products of both composites were identified. The reaction products sequence was the different-sized TiC and the coarse-grained (Ti,Nb)C+AlNb$_3$ for the SiC$_f$/C/Ti$_2$AlNb; and the fine-grained TiB$_2$+TiC, needle-shaped (Ti,Nb)B$_2$/NbB +(Ti,Nb)C, and coarse-grained (Ti,Nb)C+AlNb$_2$ for the SiC$_f$/C/B$_4$C/Ti$_2$AlNb. When the interfacial reaction process of two composites was dominated by the diffusion-controlled, the SiC$_f$/C/B$_4$C/Ti$_2$AlNb had a higher diffusion activation energy Q due to the facilitated elemental diffusion by the needle-shaped borides, making the frequency factor k_0 much larger than SiC$_f$/C/Ti$_2$AlNb, which resulted in a thicker RL in SiC$_f$/C/B$_4$C/Ti$_2$AlNb under the same consolidating conditions.

(2) The SiC$_f$/C/Ti$_2$AlNb with a thinner RL exhibited a higher interface strength than SiC$_f$/C/B$_4$C/ Ti$_2$AlNb when the interfacial debonding occurred between pyrolytic carbon and the amorphous polycrystalline structure of B$_4$C. The SiC$_f$/C/Ti$_2$AlNb with a higher interface strength exhibited a more serious step-like fracture than SiC$_f$/C/B$_4$C/Ti$_2$AlNb and thus contributed to a higher tensile strength of the SiC$_f$/C/Ti$_2$AlNb.

References

1. Larsen, J.M.; Russ, S.M.; Jones, J.W. An evaluation of fiber-reinforced titanium matrix composites for advanced high-temperature aerospace applications. *Met. Mater. Trans. A* **1995**, *26*, 3211–3223. [CrossRef]
2. Guo, Z.X.; Derby, B. Solid-state fabrication and interfaces of fiber reinforced metal matrix composites. *Prog. Mater. Sci.* **1995**, *39*, 411–495. [CrossRef]
3. Leyens, C.; Kocian, F.; Hausmann, J.; Kaysser, W.A. Materials and design concepts for high performance compressor components. *Aerosp. Sci. Technol.* **2003**, *7*, 201–210. [CrossRef]
4. Singerman, S.; Jackson, J. Titanium Metal Matrix Composites for Aerospace Applications. *Superalloys* **1996**, 579–586.
5. Mall, S. *Titanium Matrix Composites: Mechanical Behavior*; CRC Press: Lancaster, PA, USA, 1997.
6. Breuer, J.; Wilger, T.; Friesel, M.; Herzig, C. Interstitial and substitutional diffusion of metallic solutes in Ti3Al. *Intermetallics* **1999**, *7*, 381–388. [CrossRef]
7. Lütjering, G.; Williams, J.C. *Titanium*, 2nd ed.; Springer Science & Business Media: Berlin, Germany, 2007.
8. Banerjee, D.; Gogia, A.K.; Nandi, T.K.; Joshi, V.A. A new ordered orthorhombic phase in a Ti$_3$AlNb alloy. *Acta Metall.* **1988**, *36*, 871–882. [CrossRef]
9. Banerjee, D. The intermetallic Ti$_2$AlNb. *Prog. Mater. Sci.* **1997**, *42*, 135–158. [CrossRef]
10. Kumpfert, J. Intermetallic Alloys Based on Orthorhombic Titanium Aluminide. *Adv. Eng. Mater.* **2001**, *3*, 851. [CrossRef]
11. Ward-Close, C.; Minor, R.; Doorbar, P. Intermetallic-matrix composites—A review. *Intermetallics* **1996**, *4*, 217–229. [CrossRef]

12. Brunet, A.; Valle, R.; Vassel, A. Intermetallic TiAl-based matrix composites: Investigation of the chemical and mechanical compatibility of a protective coating adapted to an alumina fiber. *Acta Mater.* **2000**, *48*, 4763–4774. [CrossRef]

13. Smith, P.R.; Graves, J.A.; Rhodes, C. Comparison of orthorhombic and alpha-two titanium aluminides as matrices for continuous SiC-reinforced composites. *Met. Mater. Trans. A* **1994**, *25*, 1267–1283. [CrossRef]

14. Luo, X.; Wang, Y.Q.; Yang, Y.Q.; Zhang, M.X.; Huang, B.; Liu, S.; Jin, N. Effect of C/Mo duplex coating on the interface and tensile strength of SiC_f/Ti-21Al-29Nb composites. *J. Alloys Compd.* **2017**, *721*, 653–660. [CrossRef]

15. Yang, Y.; Zhu, Y.; Ma, Z.; Chen, Y.; Yang, Y. Formation of interfacial reaction products in SCS-6 SiC/Ti_2AlNb composites. *Scr. Mater.* **2004**, *51*, 385–389. [CrossRef]

16. Wu, M.; Zhang, K.; Huang, H.; Wang, M.; Li, H.; Zhang, S.; Wen, M. Interfacial reactions in SiC_f/C/Ti17 composites dominated by texture of carbon coatings. *Carbon* **2017**, *124*, 238–249. [CrossRef]

17. Dudek, H.J.; Borath, R.; Leucht, R.; Kaysser, W.A. Transmission electron microscopy of the fiber-matrix interface in SiC-SCS-6-fiber-reinforced IMI834 alloys. *J. Mater. Sci.* **1997**, *32*, 5355–5362. [CrossRef]

18. Gentile, M.; Xiao, P.; Abram, T. Palladium interaction with silicon carbide. *J. Nucl. Mater.* **2015**, *462*, 100–107. [CrossRef]

19. Kieschke, R.; Clyne, T. Development of a diffusion barrier for SiC monofilaments in titanium. *Mater. Sci. Eng. A* **1991**, *135*, 145–149. [CrossRef]

20. Choy, K.L. Functionally graded coatings on SiC fibers for protection in Ti-based metal matrix composites. *Scr. Mater.* **1996**, *34*, 1753–1758. [CrossRef]

21. Choy, K.L.; Durodola, J.F.; Derby, B.; Ruiz, C. Effect of TiB_2, TiC and TiN protective coatings on tensile strength and fracture behaviour of SiC monofilament fibers. *Composites* **1995**, *26*, 531–539. [CrossRef]

22. Luo, X.; Yang, Y.; Sun, Q.; Yu, Y.; Huang, B.; Chen, Y. Effect of Cu/Mo duplex coating on the interface and property of SiC_f/Ti6Al4V composite. *Mater. Sci. Eng. A* **2012**, *535*, 6–11. [CrossRef]

23. XRD and TG-DSC Analysis of the Silicon Carbide-Palladium Reaction. Available online: https://www.researchgate.net/publication/265595117_XRD_and_TG-DSC_Analysis_of_the_Silicon_Carbide-Palladium_Reaction (accessed on 25 September 2019).

24. Fu, Y.; Shi, N.; Zhang, D.; Yang, R. Effect of C coating on the interfacial microstructure and properties of SiC fiber-reinforced Ti matrix composites. *Mater. Sci. Eng. A* **2006**, *426*, 278–282. [CrossRef]

25. Huang, B.; Yang, Y.; Luo, H.; Yuan, M. Effects of the coating system and interfacial region thickness on the thermal residual stresses in SiC_f/Ti–6Al–4V composites. *Mater. Des.* **2009**, *30*, 718–722. [CrossRef]

26. Zhang, W.; Yang, Y.; Zhao, G.; Feng, Z.; Huang, B.; Luo, X.; Li, M.; Chen, Y.; Yang, Y. Interfacial reaction studies of B_4C-coated and C-coated SiC fiber reinforced Ti–43Al–9V composites. *Intermetallics* **2014**, *50*, 14–19. [CrossRef]

27. Wang, M.-J.; Huang, H.; Li, H.; Zhang, S.-M.; Wen, M.; Song, C.; Pan, F. Microstructure and interfacial strength of SiC fiber-reinforced Ti17 alloy composites with different consolidation temperatures. *Rare Met.* **2018**, *37*, 759–768. [CrossRef]

28. Zhang, S.; Wang, M.; Wen, M.; Wu, M.; Wang, Q.; Huang, H. Interfacial reactions and matrix microstructure evolution in SiC_f/Ti composites dominated by primary structure of Ti matrix. *Ceram. Int.* **2019**, *45*, 17767–17774. [CrossRef]

29. Sun, Q.; Luo, X.; Yang, Y.; Feng, G.; Zhao, G.; Huang, B.; Yang, Y. A review on the research progress of push-out method in testing interfacial properties of SiC fiber-reinforced titanium matrix composites. *Compos. Interfaces* **2015**, *22*, 367–386. [CrossRef]

30. Díaz, J.; Paolicelli, G.; Ferrer, S.; Comin, F. Separation of the sp^3 and sp^2 components in the C1 s photoemission spectra of amorphous carbon films. *Phys. Rev. B* **1996**, *54*, 8064–8069. [CrossRef]

31. Mc Evoy, N.; Peltekis, N.; Kumar, S.; Rezvani, E.; Nolan, H.; Keeley, G.P.; Blau, W.J.; Duesberg, G.S. Synthesis and analysis of thin conducting pyrolytic carbon films. *Carbon* **2012**, *50*, 1216–1226. [CrossRef]

32. Cao, X.; Shang, L.; Liang, Y.; Lu, Z.; Zhang, G.; Xue, Q. The effect of tribo-chemical reactions of mating materials on tribological behaviors of the B_4C film in various relative humidity environments. *Ceram. Int.* **2019**, *45*, 4581–4589. [CrossRef]

33. Bourrat, X.; Trouvat, B.; Limousin, G.; Vignoles, G.; Doux, F. Pyrocarbon anisotropy as measured by electron diffraction and polarized light. *J. Mater. Res.* **2000**, *15*, 92–101. [CrossRef]

34. Reznik, B.; Hüttinger, K. On the terminology for pyrolytic carbon. *Carbon* **2002**, *40*, 621–624. [CrossRef]

35. Lange's Handbook of Chemistry. Available online: https://www.researchgate.net/publication/249343603_Langes_Handbook_of_Chemistry (accessed on 17 September 2019).

36. Lihrmann, J.-M. Thermodynamics of the Al_2O_3–Al_4C_3 system: I. Thermochemical functions of Al oxide, carbide and oxycarbides between 298 and 2100K. *J. Eur. Ceram. Soc.* **2008**, *28*, 633–642. [CrossRef]

37. Hansen, M.; Kamen, E.L.; Kessler, H.D.; McPherson, D.J. Systems Titanium-Molybdenum and Titanium-Columbium. *JOM* **1951**, *3*, 881–888. [CrossRef]

38. Yang, Y.; Dudek, H.; Kumpfert, J.; Yang, Y. Interfacial reaction and stability of SCS-6 SiC/Ti–25Al–10Nb–3V–1Mo composites. *Mater. Sci. Eng. A* **1998**, *246*, 213–220. [CrossRef]

39. Yang, Y.Q.; Dudek, H.J.; Kumpfert, J. TEM investigations of the fiber/matrix interface in SCS-6 SiC/Ti–25Al–10Nb–3V–1Mo composites. *Compos. Part A: Appl. Sci. Manuf.* **1998**, *29*, 1235–1241. [CrossRef]

40. Mei, H.; Bai, Q.; Sun, Y.; Li, H.; Wang, H.; Cheng, L. The effect of heat treatment on the strength and toughness of carbon fiber/silicon carbide composites with different pyrolytic carbon interphase thicknesses. *Carbon* **2013**, *57*, 288–297. [CrossRef]